Available online at www.sciencedirect.com
SCIENCE DIRECT
Journal of Power Sources 157 (2006) 681–687
JOURNAL OF POWER SOURCES
www.elsevier.com/locate/jpowsour

Effects of silicon concentration in SOFC alloy interconnects on the formation of oxide scales in hydrocarbon fuels

Teruhisa Horita *, Haruo Kishimoto, Katsuhiko Yamaji, Natsuko Sakai, Yueping Xiong, Manuel E. Brito, Harumi Yokokawa

National Institute of Advanced Industrial Science and Technology (AIST), AIST Central 5, Higashi 1-1-1, Tsukuba 305-8565, Japan

Received 29 August 2005; received in revised form 10 January 2006; accepted 14 January 2006
Available online 24 February 2006

Abstract

Oxide scale formations on Fe–Cr alloy interconnects were investigated in anode gas (mixtures of CH_4 and H_2O) atmospheres for solid oxide fuel cells. The silicon concentration in Fe–Cr alloy changed the microstructures of oxide scales, elemental distribution and oxide scale growth rates. Oxide scale is composed of the following phases from surface to inner oxides: Fe–Mn spinel, Cr_2O_3, oxide scale/alloy interface and internal oxides of Si and Al. With decreasing the Si concentration from 0.4 to 0.01 mass%, formation of thin Si and Mn layer was observed inside the Fe–Cr alloy. Oxide scale growth rate constants decreased by lowering the Si concentration in Fe–Cr alloy from 4.2×10^{-18} to 2.1×10^{-18} $m^2\ s^{-1}$ at 1073 K. Diffusivity of Fe and Cr was changed by the concentration of Si in Fe–Cr alloy, which affects the growth rates of oxide scale. The electrical conductivity of oxidized Fe–Cr alloy shows almost same level regardless the Si concentration (in the orders of 10 S cm^{-2} at 1073 K).

Keywords: SOFCs; Fe–Cr alloy; Interconnect; Oxidation; Anode gases; GDOES

1. Introduction

In recent years, many attempts have been made on the reduction of operation temperature of solid oxide fuel cells (SOFCs) from 1273 to 1073 K or lower. For such intermediate temperature operation SOFCs, alloy materials can be applied as interconnects, which are cost-effective materials for fabrication. Among the several candidate alloys, Fe–Cr alloys have attracted much attention because of their reasonable price and high mechanical strength [1–15]. However, at operation temperatures, oxide scales are always formed on the alloy surface by the reaction with atmospheric gases. Many authors have reported the oxide scale formation in air atmospheres [1–15]. In addition, even in a fuel gas atmosphere, such as H_2–H_2O or CH_4–H_2O mixtures, several authors have reported the formation of oxide scales on the alloys [1,4,8–10,14–16]. Therefore, one critical issue for applying the Fe–Cr alloys is a formation of oxide scales on the surface at operation temperatures. We are very interested in the oxide scale formation in a fuel atmosphere because the supply of fuel with metallic components is technologically important to have stable SOFC system. The formation of insulating oxide layer is not favourable, but it is needed to have a stable protective layer. To increase the electrical conductivity of oxide scales, compositional modification of Fe–Cr alloys have been examined.

So far, several elements have been added into the Fe–Cr alloys to form Cr_2O_3-based conductive oxide layers. The addition of minor elements (such as Mn and Si) to Fe–Cr alloy gave different oxide scale formation and elemental distribution. We have reported depth profiles of elements for different kinds of oxide scales formed on Fe–Cr alloys in H_2–H_2O or CH_4–H_2O [17–21]. In the previous study [20,21], we found the following two points in relation to the formation of oxide scales in CH_4–H_2O: (i) fast diffusion of Mn in the oxide scale promotes the formation of Mn-spinel oxide on the top surface. This is important to control the oxide scale layers formation and the electrical conductivity. (ii) Si-rich phase was formed around the oxide scale/alloy interfaces, which was distributed homogeneously at the interfaces. The Si-rich part is considered to be SiO_2 oxide phase and the growth of this part is unfavourable because the insulating thick SiO_2 layer will reduce the electrical conductivity.

* Corresponding author. Tel.: +81 29 861 4542/9362; fax: +81 29 861 4540.
E-mail address: t.horita@aist.go.jp (T. Horita).

0378-7753/$ – see front matter © 2006 Elsevier B.V. All rights reserved.
doi:10.1016/j.jpowsour.2006.01.055

Table 1
Chemical composition of examined Fe–Cr alloys

	C	Si	Mn	Ni	Cr	Al	Zr	La	Fe
ZMG232	0.02	0.4	0.5	0.26	21.97	0.21	0.22	0.04	76.38
387	0.025	0.01	0.45	0.26	22.00	0.21	0.21	0.03	76.79
825	0.028	0.1	0.48	0.28	21.92	0.23	0.22	0.05	76.68

The purpose of the present study is to clarify the effects of Si concentration on the formation of oxide scales in CH_4–H_2O atmospheres. Especially three different Si concentrations were examined in the Fe–Cr alloys. The distribution of elements and growth rates of oxide scales are compared among the three different Fe–Cr alloys.

2. Experimental

2.1. Samples

The selected Fe–Cr alloys were ZMG232 (Hitachi Metals Ltd.) based alloys: ZMG232, 825 alloy and 387 alloy, which have been specially developed for SOFC interconnect by Hitachi Metals Ltd., Japan. The chemical composition of the alloys are listed in Table 1 (The alloy contains Fe and about 22 mass% of Cr with several kinds of minor elements; C, Si, Mn, Ni, Al, La and Zr.) The stability of ZMG232 has already been examined in O_2 atmosphere [6]. The electrical resistance of this alloy was only $6 \times 10^{-3}\ \Omega\,cm^2$ after operation at 1273 K for 1000 h [6]. The samples were cut into pieces in the size of about 1 cm × 1 cm, and the surfaces were polished with a diamond paste to obtain a mirror surface (up to 1/4 μm grade).

2.2. Oxidation experiments in CH_4–H_2O

The alloys were annealed at 1073 K under a H_2O saturated CH_4–Ar mixture. The mixture of CH_4 and Ar was passed through H_2O (at 50 °C) at a flow rate of 50 ml min^{-1}. The gases partial pressures before feeding to the reactor tube were as follows: $p(CH_4) = 6.0 \times 10^3$ Pa, $p(Ar) = 8.5 \times 10^4$ Pa and $p(H_2O) = 1.0 \times 10^4$ Pa. Thus, the steam/carbon ratio should be around 1.6 in this experimental condition (the calculated equilibrium partial pressure for each gas is as follows: $p(H_2) = 1.9 \times 10^4$ Pa, $p(CO) = 5.1 \times 10^3$ Pa, $p(CO_2) = 9.0 \times 10^2$ Pa, $p(H_2O) = 3.1 \times 10^3$ Pa and carbon activity, $a(C) = 0.36$). The oxidation treatments were carried out at 1073 K for 3–1032 h in an Al_2O_3-tube reactor. When the mixed gases were supplied to the reactor at 1073 K, they should be converted to CO, CO_2, H_2 and H_2O. The estimated oxygen partial pressure is around $p(O_2) = 1.3 \times 10^{-15}$ Pa. Under this condition, carbon will not be deposited according to the thermodynamic equilibrium calculation. After the experiments, there was no carbon deposited in the Al_2O_3 reactor tube. The oxide scale can be formed in the CH_4–H_2O atmosphere even at very low oxygen partial pressures. The formation of oxide scale in CH_4–H_2O can be described by the following equation when H_2O and CO_2 are the oxygen source for oxidation:

$$M + H_2O = MO + H_2 \quad (1)$$

$$M + CO_2 = MO + CO \quad (2)$$

where M is metal elements in the alloys and MO is the oxide phase formed on the alloy surface.

2.3. Analysis of oxidized alloys

Microstructures of cross-section of oxide scale were analyzed by scanning electron microscope (KEYENCE VE-7800, Japan) with EDX (Kevex, USA). The reaction phases formed on the alloy surface were identified by X-ray diffraction (Phillips PW 1800, The Netherlands).

Major and minor elements distributions in depth directions were analyzed by glow discharge optical emission spectroscopy (GDOES, JobinYvon/HORIBA, JY-5000RF) with Ar sputtering. The depth profiles were measured in an area of 2 mm in diameter. For RF generating, the following condition was selected to measure the oxide scale and alloy: pressure, 600 Pa and power 35 W. After sputtering the craters, the depths of the craters were measured by a surface profiler system (Dektak, Veeco, USA).

The electrical conductivity of oxidized alloys was measured by four-probe ac impedance measurements in the frequency range of 1 mHz to 100 kHz. Platinum paste was applied to the oxide scale surface, and the measurements were conducted in air for about 5 h. The effect of additional oxide scale growth is considered to be small because a thick oxide scale was formed for more than 1000 h oxidation.

3. Results and discussion

3.1. Microstructures of oxidized alloy surface

Fig. 1 shows microstructures of oxidized alloy surfaces after exposure to CH_4–H_2O at 1073 K for 72 and 1032 h. At the initial oxidation for 72 h, cubic or plate-like grains are observed all over the surface for the examined oxidized alloys (in Fig. 1(b, d and f)). The grain boundary parts of oxidized alloys are identified as peaks of ridges, which are high concentration of Mn determined by EDS analysis (in Fig. 1(a, c and e)) [21]. Many grain boundary lines are observed on the ZMG232 alloy (Fig. 1(a)), while relatively smooth surface on the low Si containing alloys (825 alloy in Fig. 1(c) and 387 alloy in Fig. 1(e)). Although the Mn concentration is almost the same for the examined alloys, formation of Mn-rich grain boundaries is significantly different among the examined Fe–Cr alloys. After exposure to CH_4–H_2O for 1032 h (Fig. 1(g–l)), the oxide scale surface was covered with cubic-shaped grains for all the examined alloys. The surface of oxide scale at ZMG232 alloy shows a relatively porous structure, while those at 825 alloy and 387 alloy show dense structures with cubic grains.

3.2. Microstructure of cross-section around the oxide scale/alloy interfaces

Fig. 2 shows microstructures of cross-section at the oxide scale/alloy interfaces for ZMG232, 825 alloy and 387 alloy,

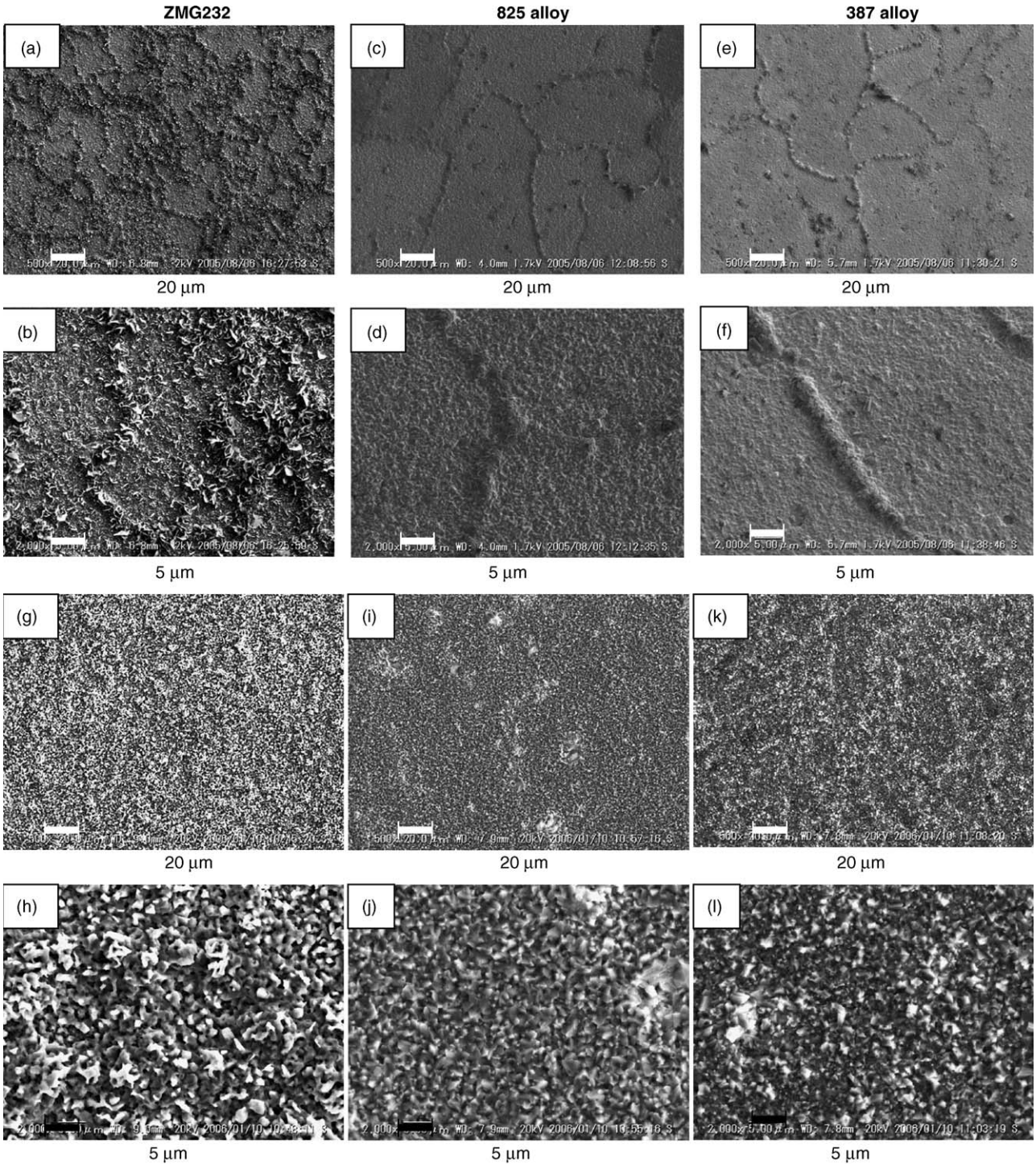

Fig. 1. Scanning electron microscope images of oxidized surfaces of Fe—Cr alloys. [Treated at 1073 K for 72 h in CH_4—H_2O: (a and b): ZMG232, (c and d): 825 alloy, (e and f): 387 alloy, treated at 1073 K for 1032 h in CH_4—H_2O, (g and h): ZMG232, (i and j): 825 alloy, (k and l): 387 alloy.]

which were treated at 1073 K for 1032 h in CH_4—H_2O. Relatively thick and dense oxide scales were formed on the alloy surfaces for all the examined alloys (thickness about 2.8–3.8 μm). The oxide scale/alloy interfaces are clear without any voids and cracks, suggesting a continuous growth of oxide scale from the alloy surfaces by diffusion process of elements. The oxide scale is identified as a zone of dark part on the surface in ZMG232 (Fig. 2a), while the other alloys show different microstructures. The characteristics of 825 and 387 alloys are summarized as follows. In the microstructures of 825 alloy (low Si concentration, Fig. 2b), a thin line is observed at the inner alloy, which is identified as Si and Mn condensed layer. Many spots are observed inside the alloys, which correspond to Al_2O_3 oxide scales. For 387 alloy (in Fig. 2c, very low Si-concentration alloy), a sim-

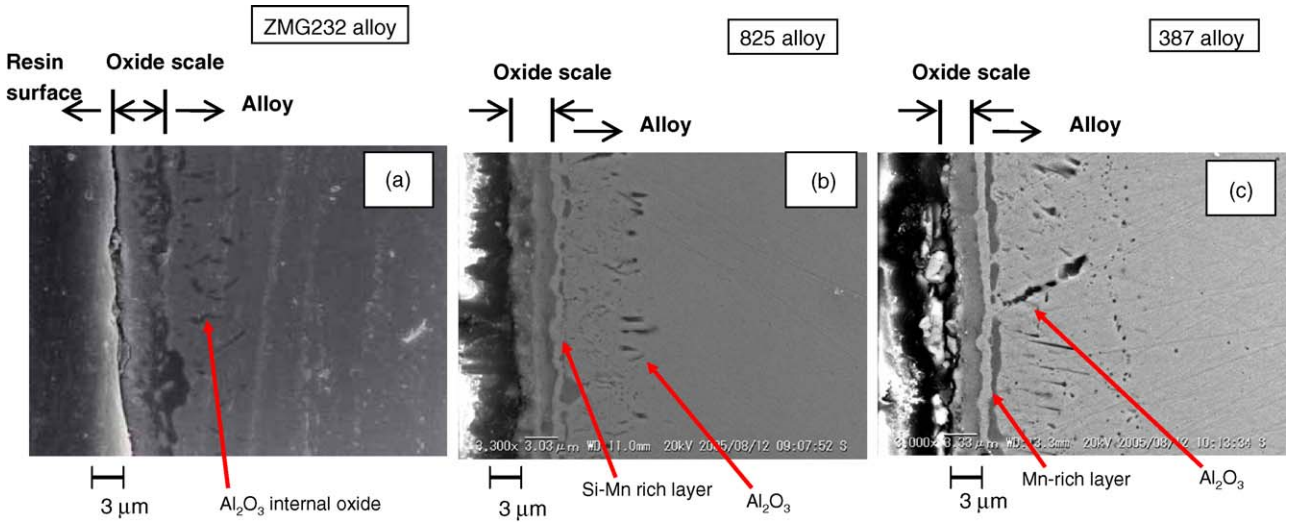

Fig. 2. Microstructures of cross-section at oxide scale/alloy interfaces treated at 1073 K for 1032 h in CH_4—H_2O. [(a): Oxidized ZMG232 alloy, (b): oxidized 825 alloy and (c): oxidized 387 alloy].

ilar thin line is observed inner alloy. This line is Mn-enriched line, not Si-enriched line as was observed in 825 alloy. The cross-sectional microstructures are different with decreasing Si concentration in Fe–Cr alloy.

3.3. Elemental distribution around the oxide scale/alloy interfaces

Fig. 3 shows depth profiles of elements around the oxide scale/alloy interfaces for the examined alloys treated at 1073 K for 1032 h. In the ZMG232 alloy (Fig. 3a), the oxide scale is identified as constant signal intensity of "O" (≈3.8 μm in depth) in the GDOES depth analysis. The following characteristics of elemental distribution are identified from surface to the oxide scale/alloy interface; Mn and Fe rich part (Mn–Fe spinel, which was confirmed by XRD), Cr_2O_3 rich part, Si condensed part and Al_2O_3 internal oxides in Fe–Cr alloy. This distribution is consistent with the observed microstructure in the cross-section (Fig. 2a). In the 825 alloy (Fig. 3b), the following phases are identified from surface to inner oxide; Mn and Fe rich part (Fe–Mn spinel), Cr_2O_3 rich part, Fe–Cr–Ni rich part (alloy part), Si and Mn condensed part and Al_2O_3 internal oxides and Fe–Cr alloy. A significant difference is observed in the distributions of Si and Mn between ZMG232 and 825 alloy. Si and Mn are condensed as the oxide form in the Fe–Cr alloy. In the 387 alloy (Fig. 3c, very low Si concentration Fe–Cr alloy), the elemental distribution is similar to low Si alloy (825 alloy). The identified phases are Fe–Mn rich part, Cr_2O_3 rich part, Fe–Cr–Ni alloy, Mn condensed part and Al_2O_3 internal oxides and Fe–Cr alloy. In the oxide scale close to the surface region, oxide scale is composed of a similar oxides from surface to inner part regardless the Si concentration. The difference between 825 and 387 alloys is the distribution of Si in the Fe–Cr alloy. Although 387 alloy contains 0.01 mass% of Si, the GDOES profile shows the detection limit level (Fig. 3c), which is very difficult to determine the distribution of Si around the oxide scale/alloy interface.

For the formation of Si and Mn thin oxide line in the Fe–Cr alloy, equilibrium oxygen partial pressure between metal and oxide is considered. If we assume the following oxidation reaction for Si and Mn, the equilibrium oxygen partial pressures between metal and oxide can be derived from the calculations:

$$\mathrm{Si(sl)} + \mathrm{O_2(g)} = \mathrm{SiO_2(s)} \quad (3)$$

$$\mathrm{Mn(sl)} + \tfrac{1}{2}\mathrm{O_2(g)} = \mathrm{MnO(s)} \quad (4)$$

$$\mathrm{Mn(sl)} + \tfrac{2}{3}\mathrm{O_2(g)} = \tfrac{1}{3}\mathrm{Mn_3O_4(s)} \quad (5)$$

The equilibrium constant for each reaction at 1073 K is $K_3 = 9.0 \times 10^{34}$ for Eq. (3), $K_4 = 7.8 \times 10^{14}$ for Eq. (4) and $K_5 = 3.0 \times 10^{16}$ for Eq. (5), respectively. Thus, the equilibrium oxygen partial pressures between metal/oxide are calculated assuming the activities of each metal is unity: $p(O_2) = 1.1 \times 10^{-35}$ bar (1.1×10^{-30} Pa) for Eq. (3), $p(O_2) = 1.6 \times 10^{-30}$ bar (1.6×10^{-25} Pa) for Eq. (4) and $p(O_2) = 1.9 \times 10^{-25}$ bar (1.9×10^{-20} Pa) for Eq. (5). The oxygen partial pressures for Eqs. (3) and (4) are lower than the equilibrium of Cr/Cr_2O_3 ($p(O_2) = 1.4 \times 10^{-28}$ bar (1.4×10^{-23} Pa)). This suggests that the formation of SiO_2 and MnO oxides should be inside the Cr_2O_3 oxide scales on Fe–Cr alloy, where the lower oxygen partial pressure is assumed inside the oxide scale (Fig. 3). Although Mn_3O_4 oxide is most probable oxide form for Mn–oxide, the stable oxide phase in the lower oxygen partial pressure is assumed to be MnO inside the Cr_2O_3 based oxide scale on Fe–Cr alloy. For determining the precise oxide scale phases, we need more data to understand the reaction phases. We will report this point in the near future.

3.4. Oxide scale growths for oxide scales

The oxide scale thickness was estimated from the distribution of O in the GDOES depth profiles. A constant intensity of O signal part is identified as oxide scale thickness. Fig. 4 shows

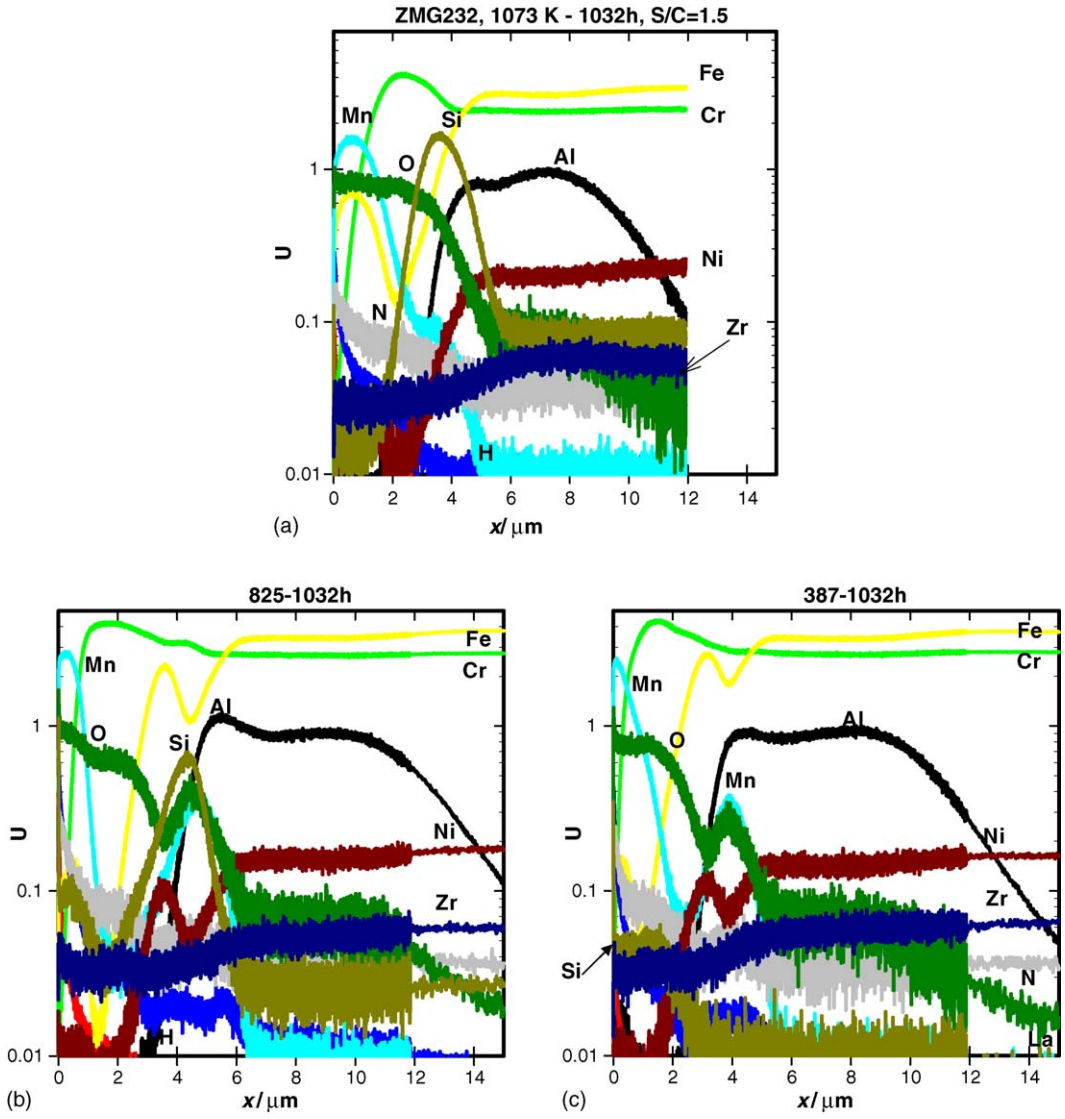

Fig. 3. Depth profiles of elements around the oxide scale/alloy interfaces treated at 1073 K for 1032 h in CH_4–H_2O. [(a): ZMG232, (b): 825 alloy and (c): 387 alloy].

oxide scale thickness as a function of annealing time for three different Fe–Cr alloys. The growth of oxide scale obeys the parabolic growth relationship, which is described as follows:

$$x^2 = k_p t \tag{6}$$

where x is the thickness of oxide scale formed on the alloys, k_p the parabolic growth rate constant and t is the annealing time for oxide scale. From the slopes of the fitting lines, the growth rate constants are calculated for each oxide scale formed on the alloys; $k_p = 4.2 \times 10^{-18}\,m^2\,s^{-1}$ for ZMG232, $2.9 \times 10^{-18}\,m^2\,s^{-1}$ for 825 alloy and $2.1 \times 10^{-18}\,m^2\,s^{-1}$ for 387 alloy. The growth rate constants decreased with lowering the Si concentration in Fe–Cr alloys. This suggests that a reduction of Si concentration in Fe–Cr alloy affects the diffusivity of Fe and Cr in Fe–Cr alloy, which eventually reduces the oxide scale growth rates. Minor additions of Si and Mn can also change the microstructures of oxide scales, which affect the diffusivity of Fe and Cr in the oxide scales and in the Fe–Cr alloy (Fig. 4).

3.5. Electrical conductivity of oxidized alloy

Fig. 5 shows electrical conductivity of oxidized alloys as a function of inverse temperatures. The electrical conductivity shows semi-conductor temperature dependence, which is mainly contributed from oxide scales formed on the alloys. The electrical conductivity of the examined alloy was in the range of 0.05–0.1 S cm^{-2} at 1073 K. The electrical conductivity shows a similar order of the magnitude for all the examined alloys. No distinct effect of Si reduction was observed in the oxide scales formed on Fe–Cr alloy surface. From the slopes of the electrical conductivity, we can estimate the activation energy for electrical conduction. The calculated activation energy is 0.67 eV for ZMG232, 0.90 eV for 825 alloy and 1.0 eV for 387 alloy. The difference of activation energy can come from the composition of oxide scale, thickness of oxide scale and formed structures in the oxide scales. The formation of thin Si and Mn layer inside the Fe–Cr alloy can also affect the electrical conduction properties. The electrical conductivity obtained in this study shows almost

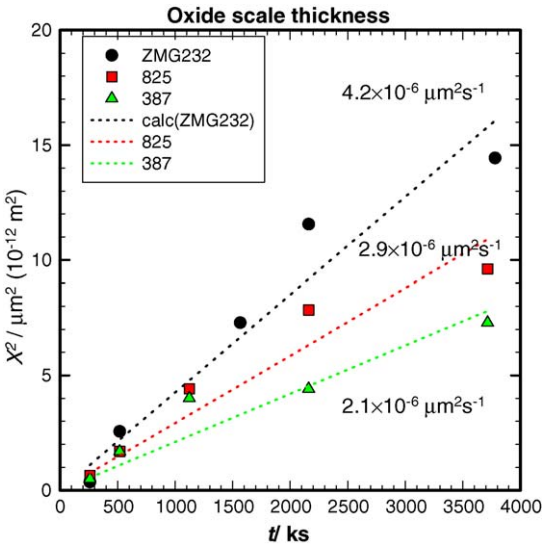

Fig. 4. Oxide scale thickness as a function of annealing time for three different Fe–Cr alloys treated at 1073 K in CH_4–H_2O. [(●): ZMG232, (●): 825 alloy, (▲): 387 alloy, the slopes indicate the growth rate constants (k_p) for each alloy; $k_p = 4.2 \times 10^{-18}$ m^2 s^{-1} for ZMG232, 2.9×10^{-18} m^2 s^{-1} for 825 alloy, 2.1×10^{-18} m^2 s^{-1} for 387 alloy].

same level those reported in the previous study [14,15] both in oxidizing and reducing atmospheres. This is because the similarity of oxide scale phases formed on ZMG232 based alloys for both atmospheres.

3.6. Application to the real SOFC stack operation

The present results suggested that controlling the Si concentration in Fe–Cr alloy could change the oxide scale composition and the growth rate of oxide scale. In a real SOFC operation, the Fe–Cr alloy interconnects contact with oxide based electrode and Ni–oxide cermet under current flow condition. The oxide scale in a real operation condition may be somewhat different from the present results because of the interface diffusion of elements between Fe–Cr alloy and electrodes. However, this work suggests the basic oxidation mechanism on Fe–Cr alloy. At least, controlling the Si concentration is one of the important factors to have stable Mn-spinel and Cr_2O_3 based oxide scales on Fe–Cr alloy interconnects.

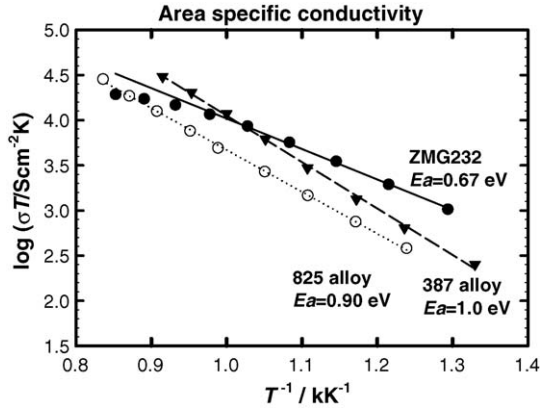

Fig. 5. Electrical conductivity of oxidized alloys as a function of inverse temperature. [Oxidation at 1073 K for 1032 h in CH_4–H_2O. (●): ZMG232, (◯): 825 alloy, (▼): 387 alloy].

4. Conclusion

Oxide scales formation was investigated on Fe–Cr alloy interconnects in CH_4–H_2O atmosphere at 1073 K. Concentration of Si changed the microstructures of oxide scales, elemental distribution and oxide scale growth rates. Oxide scale formed is composed of the following phases from surface to inner oxides: Fe–Mn spinel, Cr_2O_3 rich part, oxide scale/alloy interface and internal oxides of Al and Si. Formation of thin Si and Mn layers were observed as internal oxides inside the Fe–Cr alloy in the lower Si concentration Fe–Cr alloy. Oxide scale growth rates decreased by lowering the Si concentration in Fe–Cr alloy. Diffusivity of Fe and Cr was changed by the concentration of Si, which affects the growth rates of oxide scale. The electrical conductivity of oxidized Fe–Cr alloy shows almost same level regardless the Si concentration (about 10 S cm^{-2} at 1073 K).

Acknowledgements

The authors are grateful to Dr. Uehara and Dr. Toji (Hitachi Metals Ltd.), Dr. Sakurai, Dr. Matsuzaki, Dr. Ogasawara, and Dr. Kameda (Tokyo Gas Co.), for their valuable comments and discussions.

References

[1] W.J. Quadakkers, T. Malkow, J. Piron-Abellan, U. Flesch, V. Schemet, L. Singheiser, in: A.J. McEvoy (Ed.), Proceedings of Fourth European SOFC Forum, The European SOFC Forum, Switzerland, 2000, p. 827.
[2] Y. Matsuzaki, I. Yasuda, Solid State Ionics 132 (1999) 271.
[3] M. Ueda, M. Kadowaki, H. Taimatsu, Mater. Trans., JIM 41 (2) (2000) 317.
[4] T. Brylewski, M. Nanko, T. Maruyama, K. Przybylski, Solid State Ionics 143 (2001) 131.
[5] K. Huang, P.Y. Hou, J.B. Goodenough, Solid State Ionics 129 (2000) 237.
[6] T. Uehara, T. Ohno, A. Toji, in: J. Huijsmans (Ed.), Proceedings of the Fifth European SOFC Forum, European Fuel Cell Forum, 2002, p. 281.
[7] T. Uehara, A. Toji, K. Inoue, M. Yamaguchi, T. Ohno, in: S.C. Singhal, M. Dokiya (Eds.), Solid Oxide Fuel Cells VIII, PV2003-07, The Electrochemical Society Inc., Pennington USA, 2003, p. 914.
[8] N. Dekker, B. Rietveld, J. Laatsch, F. Tietz, in: M. Mogensen (Ed.), Proceedings of Sixth European SOFC Forum, The European SOFC Forum, Switzerland, 2004, p. 319.
[9] T.F. Pederson, S. Linderoth, J. Laatsch, in: M. Mogensen (Ed.), Proceedings of Sixth European SOFC Forum, The European SOFC Forum, Switzerland, 2004, p. 897.
[10] M. Kuznecov, K. Eichler, S. Megel, P. Otschik, in: M. Mogensen (Ed.), Proceedings of Sixth European SOFC Forum, The European SOFC Forum, Switzerland, 2004, p. 1573.
[11] P. Huczkowski, N. Christiansen, V. Shemet, L. Singheiser, W.J. Quadakkers, in: M. Mogensen (Ed.), Proceedings of Sixth European SOFC Forum, The European SOFC Forum, Switzerland, 2004, p. 1594.
[12] W. Glatz, G. Kunschert, M. Janousek, A. Venskutonis, SOFC-XI, PV2005-07, in: S.C. Singhal, J. Mizusaki (Eds.), Electrochemical Society, Proceedings Series, Pennington, NJ, 2005, p. 1773.
[13] A. Toji, T. Uehara, T. Ohno, SOFC-XI, PV2005-07, in: S.C. Singhal, J. Mizusaki (Eds.), The Electrochemical Society, Proceedings Series, Pennington, NJ, 2005, p. 1789.

[14] J.W. Fergus, Mater. Sci. Eng. A 397 (2005) 271.
[15] J.W. Fergus, SOFC-XI, PV2005-07, in: S.C. Singhal, J. Mizusaki (Eds.), The Electrochemical Society, Proceedings Series, Pennington, NJ, 2005, p. 1806.
[16] D.M. England, V. Vilkar, J. Electrochem. Soc. 148 (4) (2001) A330.
[17] T. Horita, Y. Xiong, K. Yamaji, N. Sakai, H. Yokokawa, in: J. Huijsmans (Ed.), Proceedings of the Fifth European SOFC Forum, European Fuel Cell Forum, 2002, p. 401.
[18] T. Horita, Y. Xiong, K. Yamaji, N. Sakai, H. Yokokawa, J. Electrochem. Soc. 150 (3) (2003) A243.
[19] T. Horita, Y. Xiong, K. Yamaji, N. Sakai, H. Yokokawa, J. Power Sources 118 (1–2) (2003) 35.
[20] T. Horita, Y. Xiong, H. Kishimoto, K. Yamaji, N. Sakai, H. Yokokawa, J. Power Sources 131 (2004) 293.
[21] T. Horita, Y. Xiong, K. Yamaji, H. Kishimoto, N. Sakai, H. Yokokawa, Solid State Ionics 175 (1–4) (2004) 157.